

Quantitative modeling and experimental verification of Förster Resonant Energy Transfer in upconversion nanoparticle biosensors

Ananda Das,^{1, a)} Conrad Corbella Bagot,^{2, a)} Eric Rappeport,^{2, a)} Taleb Ba Tis,³ and Wounjhang Park^{2, 3, b)}

¹⁾*Department of Physics, University of Colorado, Boulder CO 80309-0390, U.S.A*

²⁾*Department of Electrical, Computer, and Energy Engineering, University of Colorado, Boulder, CO 80309-0425, U.S.A*

³⁾*Materials Science and Engineering, University of Colorado, Boulder, CO 80309, U.S.A*

(Dated: 16 June 2021)

Rare-earth doped upconversion nanoparticles (UCNPs) have often been used in combination with fluorescent dyes for sensing applications. In these systems, sensing can be achieved by the modulation of Förster resonant energy transfer (FRET) between the dye and the UCNP. The effects of FRET in such cases are complex, as the extent to which FRET is experienced by the rare-earth ions is dependent on their position within the nanoparticle. Here, we develop an analytical model to accurately describe the effects of FRET for such a system. As a proof of principle, we verify our model by considering the case of a pH sensor comprised of Fluorescein Isothiocyanate and Tm³⁺ doped UCNPs. We extend our model to the case of core-shell UCNPs and discuss the design of an optimal FRET based biosensor using UCNPs.

^{a)}These authors contributed equally to this work

^{b)}Corresponding author; won.park@colorado.edu

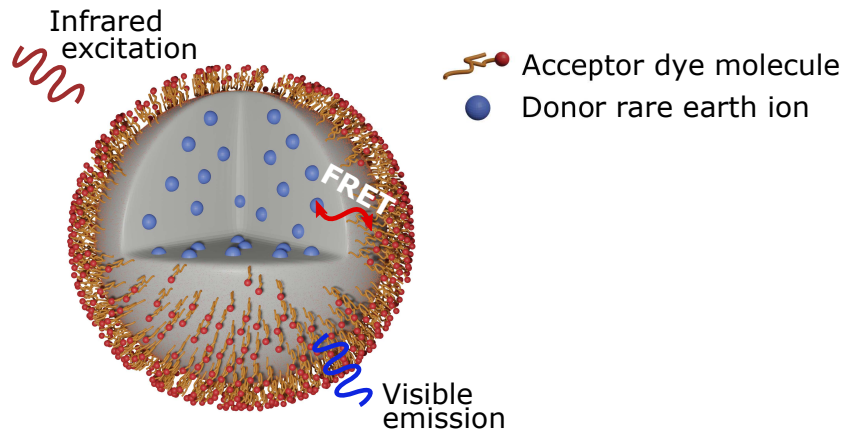


FIG. 1: General schematic of a dye conjugated UCNP sensor. The fluorescent dye's absorption spectrum matches the UCNP emission spectrum and changes in the presence of the target being sensed. Sensing is achieved by monitoring the modulation in UCNP emission intensity by the dye under infrared excitation.

I. INTRODUCTION

Upconversion nanoparticles (UCNPs) have been a major topic of research in the biomedical field due to their striking advantages as bioimaging agents. UCNPs are excited by infrared light which falls in the biological transparency window and thus penetrates deeper into the body. Furthermore, the infrared excitation does not excite any background tissue fluorescence and does not lead to photobleaching or photoblinking that commonly occurs in conventional fluorescent dyes or quantum dots. Because of these appealing properties, UCNPs have been studied for frontier applications, including information security¹, bioimaging²⁻⁵, and therapeutic purposes⁶⁻¹⁰.

The strengths of UCNPs as bioimaging agents extend quite naturally to biosensing applications. UCNPs have been used in a number of sensing schemes for DNA¹¹⁻¹³, biomolecules¹⁴⁻¹⁶, metal ions¹⁷⁻¹⁹, and physiological indicators such as pH²⁰⁻²³. Figure 1 shows a schematic of a typical UCNP based sensor. The sensor is comprised of a UCNP whose surface is covered with a fluorescent dye molecule. The dye is chosen such that its absorption spectrum changes in the presence of the analyte being sensed. By doping the UCNP with a rare-earth ion whose emission band overlaps with the absorption band of the fluorescence molecule, it is possible to achieve sensing by reading out the changes in UCNP emission intensity under infrared excitation.

Changes in UCNP emission from the conjugated dye can occur in two ways. One way is through radiative transfer where the UCNP emits photons which then get reabsorbed by dye molecules within the emission path. This has also been referred to in the literature as ‘the inner filter effect’^{24–26}. The second way is through nonradiative Förster Resonant Energy Transfer (FRET) between the UCNP and the molecules attached to its surface^{14,27–30}. A FRET-based sensor is preferable to one that uses radiative transfer as the dominant mechanism because FRET can result in much stronger modulation of luminescence, leading to higher sensitivity. Furthermore, the extremely short range of influence for FRET results in highly localized sensing that is much more robust against environmental noise.

While FRET-based sensing schemes have a long, rich history of research and development^{31–33}, most of the discussion typically considers the interactions between a single donor-acceptor pair. For FRET-based sensing with UCNPs, the situation is much more nuanced as we now not only have multiple donors to consider (the rare earth ions within the UCNP) but also have multiple acceptors (the dye molecules attached to the surface) affecting each donor. As a result, the FRET modulated emission from the donor ions in the UCNPs varies depending on where in the nanoparticle the ion is located. Donors close to the surface of the UCNP experience strong FRET while those in the core of the particle might not be affected by FRET at all. As a further complication, it is a common practice to grow an inert shell over the UCNPs to negate the effects of surface defects and achieve brighter upconversion emission^{34,35}. For FRET-based sensors using these core-shell UCNPs, now all donor ions have an additional layer of separation between them and the acceptor molecules on the surface. The effects of this separation on the sensitivity of such a system are not well understood and, as a result, the rational design of an optimal sensor is not possible. While some modeling of nanoparticle-based FRET systems has been developed^{36,37}, the use of such models towards sensor design and optimization remains under-explored.

In this paper, we develop an analytical model that captures the effects of FRET for the case of dye conjugated UCNPs commonly used in sensing applications. We start from the well-established theory of a single donor-acceptor pair case and extend the theory to the case of a sphere of donors surrounded by a uniform surface density of acceptors. Using the basic underlying principles of FRET, we show that it is possible to come up with a purely analytical description for the FRET experienced by a donor at any point within the sphere. The model depends on only a few easily measurable variables and thus removes the need for

exhaustive experimental studies when designing the optimal sensor. Furthermore, it does not suffer from scalability issues that naturally arise from brute force Monte Carlo simulations that have been used to describe such systems. We also experimentally monitor the effects of FRET on Tm^{3+} UCNP conjugated with Fluorescein Isothiocyanate (FITC), a FRET-based system that has been used for pH sensing^{22,23,38,39}. We show good agreement between the theory developed and the experimental results thus demonstrating the validity of the theory for FRET-based sensing in dye conjugated UCNP systems. Finally, we extend the analysis to core-shell configurations and discuss the design of an optimal UCNP biosensor using this model.

II. THEORY

We start with the standard FRET equation for a donor-acceptor pair separated by a distance r . The FRET efficiency in this case is given by:

$$E = \frac{k_{ET}}{k_f + k_{ET} + k_{NR}} = \frac{1}{1 + \left(\frac{r}{R_0}\right)^6} \quad (1)$$

where k_{ET} is the rate of energy transfer between the donor and the acceptor, k_f is the radiative decay rate of the donor and k_{NR} is the nonradiative decay rate of the donor³³. As shown in Eq. 1, the FRET efficiency can also be expressed as a function of the Förster radius R_0 , which is defined as the distance where the FRET efficiency is 50%. The Förster radius for a donor-acceptor pair can be calculated by considering a variety of factors such as the spectral overlap between the donor emission spectrum and acceptor absorption spectrum, the quantum efficiency of the donor, and the surrounding index of refraction (see Supplementary Information (SI) 1). We can express the energy transfer rate in terms of the Förster radius as follows:

$$k_{ET} = \left(\frac{R_0}{r}\right)^6 k_0 \quad (2)$$

where k_0 is the total decay rate of the donor in the absence of the acceptor. Equations 1 and 2 are all that is required to fully describe a single donor-acceptor pair. For the case of a donor in the presence of multiple acceptors we can make use of the fact that decay rates are additive. Thus, for a donor surrounded by N acceptors all a distance r away, the total

energy transfer rate is

$$k_{ET} = \sum_{i=0}^N \left(\frac{R_0}{r_i} \right)^6 k_0 = N \left(\frac{R_0}{r} \right)^6 k_0 \quad (3)$$

In this scenario we see the ‘antenna effect’³³ where one can define a larger effective Förster radius (i.e $R_{0,\text{eff}} = N^{\frac{1}{6}} R_0$), which scales nonlinearly with the number of acceptor molecules.

We now consider the case of a donor within a sphere of radius R , where the donor is at radial coordinate a . The sphere is covered with N acceptor ions uniformly distributed across the surface of the sphere (See Fig. 2a). To calculate the full energy transfer rate for such a donor, we first note that all acceptors on the infinitesimal cylinder slice shown in Figure 2a are an equal distance ξ from the donor. Using Eq. 3, we can then calculate the contribution to the total energy transfer rate from all the acceptors in this slice as:

$$k_{ET,dA} = \sigma dA \left(\frac{R_0}{\xi} \right)^6 k_0 \quad (4)$$

where σ is the density of acceptor molecules on the surface and dA is the area of the infinitesimal cylinder shown in Figure 2a.

To get the full energy transfer rate, we calculate the contribution from all such infinitesimals by integrating over θ and we get:

$$k_{ET} = \int_0^\pi k_0 \left(\frac{R_0}{r(\theta)} \right)^6 \frac{N}{4\pi R^2} 2\pi R^2 \sin(\theta) d\theta \quad (5)$$

Using a change of variables (see SI 2), this integral can be analytically solved to get:

$$k_{ET} = \frac{\bar{a}^2 + 1}{(\bar{a}^2 - 1)^4} N \left(\frac{R_0}{R} \right)^6 k_0 \quad (6)$$

where \bar{a} is the position of the donor within the sphere relative to the radius of the sphere ($\bar{a} = a/R$). Comparing Equation 6 to Equations 2 and 3, we can see both the expected ‘antenna effect’ due to multiple acceptors as well as a prefactor that arises from the spherical geometry of the problem. The resultant FRET efficiency experienced by the donor can be calculated as:

$$E = \frac{k_{ET}}{k_{ET} + k_0} = \frac{1}{1 + \frac{(\bar{a}^2 - 1)^4}{\bar{a}^2 + 1} \frac{1}{N} \left(\frac{R}{R_0} \right)^6} \quad (7)$$

where once more we can see the ‘antenna effect’ scaling term as well as the geometric prefactor.

Thus, using only knowledge of the size of the particle, the Förster radius, and the number of acceptor molecules attached to the surface, it is possible to calculate the FRET efficiency

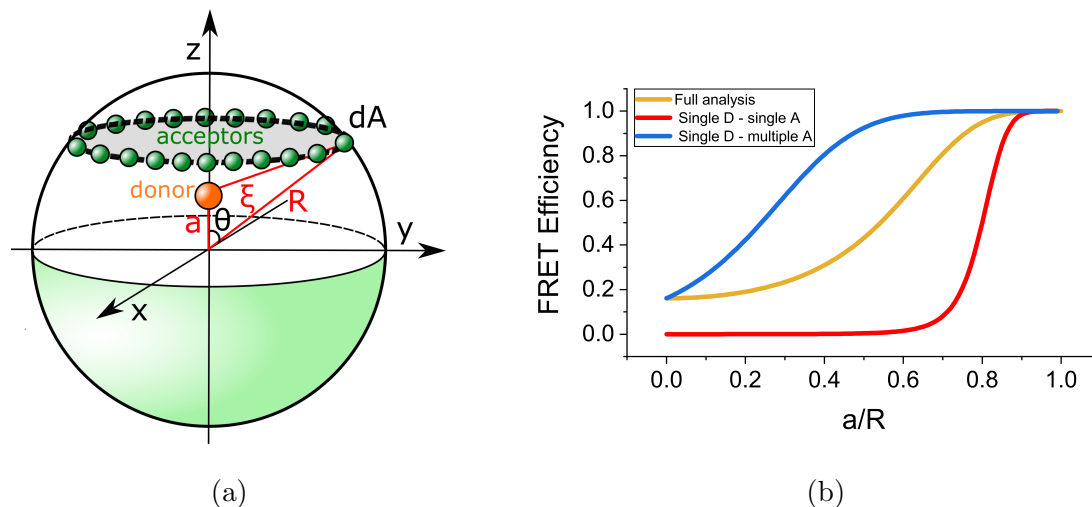


FIG. 2: (a) A donor (in orange) at radius a away from the center of the nanoparticle experiences FRET from all equidistant acceptors (in dark green, a distance ξ away from the donor) on the surface of an infinitesimal cylinder with area dA . The total FRET experienced by the donor can be calculated by summing over the contributions from all such cylinders. (b) FRET efficiency obtained with the full analysis suggested in this paper compared to that obtained with a single donor - single acceptor model, and a single donor - multiple acceptors model. Only the full analysis adequately captures the efficiency of the interaction. A denotes acceptors, and D denotes donors.

of a donor ion anywhere within the particle. Figure 2b shows the FRET efficiency for a donor ion as a function of normalized radial position within the particle using typical parameters for a UCNP-dye biosensor. We assume a particle radius of 15 nm, Förster radius of 3 nm and surface density of 3000 molecules per particle. Note that despite that radius being 5 times the Förster radius, donor ions near the core of the UCNP still experience non-negligible FRET due to the ‘antenna effect’. Also, as expected, donors near the edge experience significantly more FRET than donors close to the center. As crude estimates, we also plot FRET efficiencies for a single donor-acceptor pair, and between a single donor and 3000 acceptor molecules. Clearly, these simpler models either overestimate or underestimate the effects of FRET for such a system and thus the full analysis is necessary.

The total luminescence intensity and decay waveform can now be obtained by integrating Eq. 7 over the entire UCNP volume (see SI 3). These quantities are then compared with the experimental results, as discussed later. We may further consider how the distribution

of ions within the particle affects the overall emission from the UCNP-dye biosensor. If we divide the UCNP into infinitesimal shells with an even distribution of donor ions, the outer shells contribute a lot more to luminescence output than the inner shells purely because they have more ions within them. Since these outer shells are more affected by FRET, it is possible that, for certain values of R , R_0 and N , the effects of FRET dominate the signal from the UCNPs. However, for large particle size, small Förster radius and/or poor dye coverage, there might be negligible effects from FRET as the signal from the unaffected inner shell ions dominates. This further illustrates the importance of considering the full theoretical analysis to determine which scenario applies for a particular choice of UCNP-dye pair in a sensing application. The analysis shown here can be easily extended to core-shell configurations simply by offsetting the distance between the donor and the surface by the shell thickness.

III. RESULTS

A. Verification of the theory

To experimentally verify the developed theory for dye-UCNP FRET interactions, we performed photoluminescence lifetime measurements on a dye-conjugated UCNP system that has previously been used as a pH sensor^{22,23,38,39}. For our study, we use UCNPs with a NaYF₄ host matrix doped with 24.7% Yb³⁺ and 0.3% Tm³⁺ as sensitizer and activator ions, respectively. NaYF₄ is a commonly used host matrix due to its low phonon energy and doping with Yb³⁺ as a sensitizer ion is standard practice to enhance the upconversion emission from Tm³⁺. To investigate the dependence on particle size, we use nanoparticles of two different sizes. As seen in the transmission electron microscope (TEM) images in Figure 3a and 3b, the nanoparticles are monodispersed with measured radii of 20.8 ± 1.1 nm and 13.7 ± 0.5 nm. Figure 3c shows a typical photoluminescence spectrum (PL) from the nanoparticles upon 980 nm excitation along with the energy level diagram for the upconversion process. The nanoparticles have a strong emission line at 475 nm which stems from a three photon upconversion excitation process to the ¹G₄ state of Tm³⁺.

In order to see the effects of FRET, we require a dye with an absorption line that overlaps the UCNP emission spectrum. For our study, we use FITC, which has strong absorption

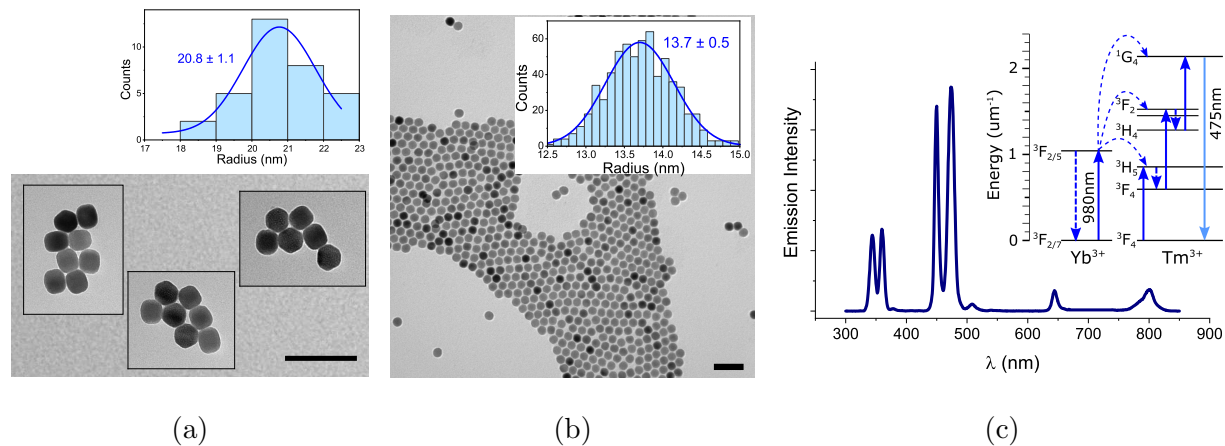


FIG. 3: Representative TEM images and size distribution of the 21 (a), and 14 nm (b) radius UCNP. Black lines in the bottom right corner represent 100 nm. (c) Typical spectrum of synthesized particles under 980 nm excitation. In the figure inset, a simplified energy-level diagram for the Tm^{3+} UCNP is presented. In the experiments performed for this paper, the lifetime of the 475 nm transition is compared across samples with different concentrations of FITC and diameters.

at blue wavelengths. The structure of FITC molecules is reversibly altered by changes in pH. At low pH values, it is spirocyclic and does not present fluorescence. As the pH is increased, it becomes open-ringed and shows fluorescence²³ (see Fig. 4a). This makes FITC a useful pH-sensor. However, photo-bleaching under ultraviolet (UV) excitation⁴⁰ and its easy release from cells have limited the use of FITC as a pH-sensor in biological applications. An FITC-UCNP sensing system is thus advantageous as, by avoiding the UV excitation of FITC, the photo-bleaching issue is eliminated. Using a UCNP-dye sensor also lends itself to further conjugation with targeting molecules, e.g. antibodies, for specific binding with cells¹⁰. After accounting for the spectral overlap and other relevant factors (see SI 1 for the calculation) we estimate a Förster radius of 3.3 nm for the FITC- Tm^{3+} pair.

The FITC was conjugated with the UCNP using a two-step ligand exchange protocol described in detail in the methods section. Equation 7 in the previous section shows that the FRET efficiency is dependent on the number of acceptor molecules attached to the surface and the ratio of Förster radius to particle radius. We can therefore test the full range of parameters of the theory by varying the size of the UCNP and the number of FITC molecules attached onto the UCNP surface. The number of FITC molecules attached is easily

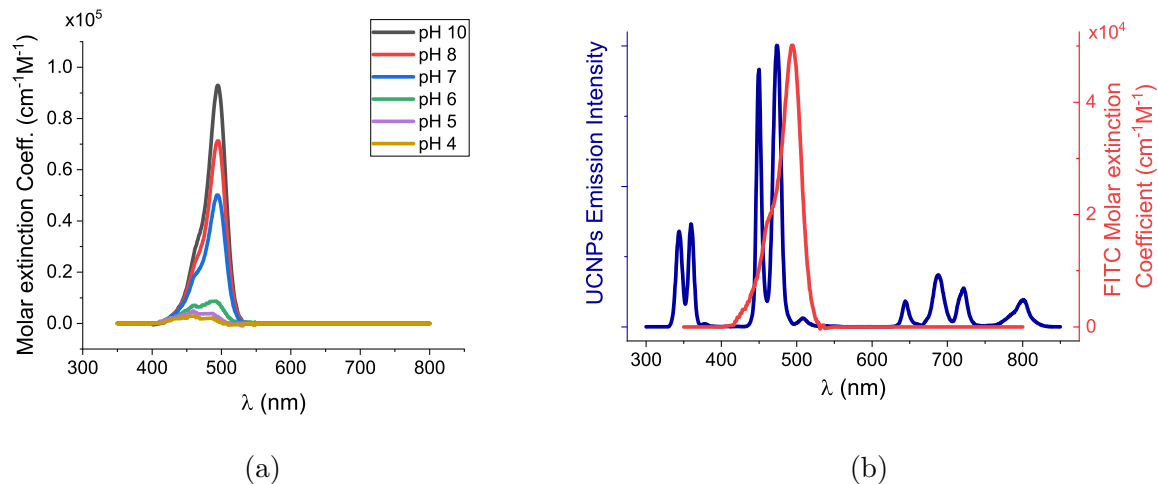


FIG. 4: (a) Absorption spectra of FITC dissolved in different pH buffers. As the pH becomes more basic, the FITC absorption increases. (b) Comparison of the UCNPs emission and the FITC absorption profile in pH 7 buffer. The FITC absorption spectrum overlaps with the 475nm 1G_4 transition of Tm^{3+} resulting in a high FRET efficiency at that wavelength.

controlled by adjusting the mass of FITC added during the conjugation step. According to the theory established in the previous section, we expect that, as the number of FITC molecules is increased, the effects of FRET should become more prominent for our dye-UCNP system. Additionally, we expect a stronger FRET effect for the smaller particles as the donor ions within them are on average closer to the acceptor molecules.

Figures 5a and 5b show the upconversion luminescence lifetime signals measured at 475 nm for the various dye-conjugated UCNP systems in Dimethylformamide (DMF) solution. We also plot the transient PL signal of the particles without any FITC. Additionally, the measured photoluminescence spectra for the 14nm nanoparticles with different FITC loadings can be found in the SI 5.

In the absence of FITC, the larger UCNP systems had a lifetime τ of 61515 μs , and the smaller particles had a lifetime of 58510 μs . The particles lack inert shells, so the slight decrease in lifetime of the smaller particles is expected due to additional nonradiative loss from surface defects. With the addition of FITC, a clear increase in decay rate ($1/\tau$) can be seen for all cases, and the samples with more FITC decay faster, as expected. We can also see a difference across the two sizes, where the smaller particle's decay rate increases by a lot more

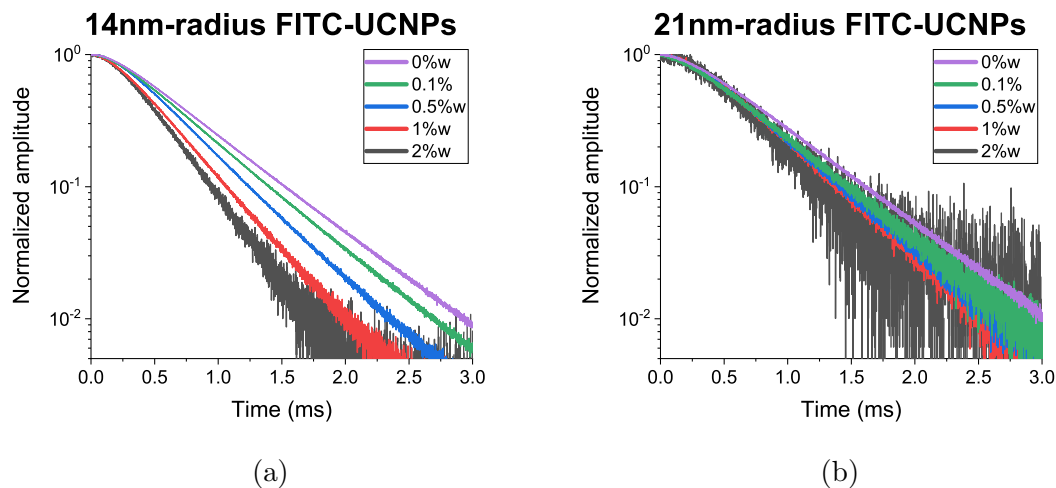


FIG. 5: Time decay measurement profiles for FITC-UCNPs with (a) 14 nm and (b) 21 nm particle radius, and different weight concentrations of FITC. As the weight concentration of FITC increases, the decay rate increases. For comparable FITC loadings, the smaller 14nm radius UCNPs experience a larger rate increase as the donor rare earth ions within them are on average closer to the acceptor FITC molecules.

than the larger particle for a comparable loading of FITC.

To verify that the theory accurately captures the decay dynamics observed, we plot the measured decay along with the predicted decay from theory in Figure 6. For our analysis, we only consider decay starting at 1 ms. At that point, any residual upconversion due to energy transfer from Yb ions has been completed, and the UCNP luminescence is purely decaying⁴¹. Figure 6a and 6b show the normalized time decays from Figure 5 between 1 ms and 2 ms for particles of both sizes. We also plot the predicted theoretical decay curves from our model in black. The decay curves have been offset on the y-axis for easier viewing. According to the theory, the decay should depend on the number of FITC molecules, the particle radius, and the Förster radius. Note that these three parameters were verified by completely independent means and no parameters were fit for to match the experimental results to theory.

The FITC-UCNP decay cannot be modeled as a single exponential as each donor ion's decay rate depends on its position within the particle (see SI 3). However, we can extract an effective time constant by integrating the transient PL curve over time. We can compare this effective time constant to the time constant in the absence of acceptor molecules to

This is the author's peer reviewed, accepted manuscript. However, the online version of record will be different from this version once it has been copyedited and typeset.
PLEASE CITE THIS ARTICLE AS DOI: 10.1063/5.0053464

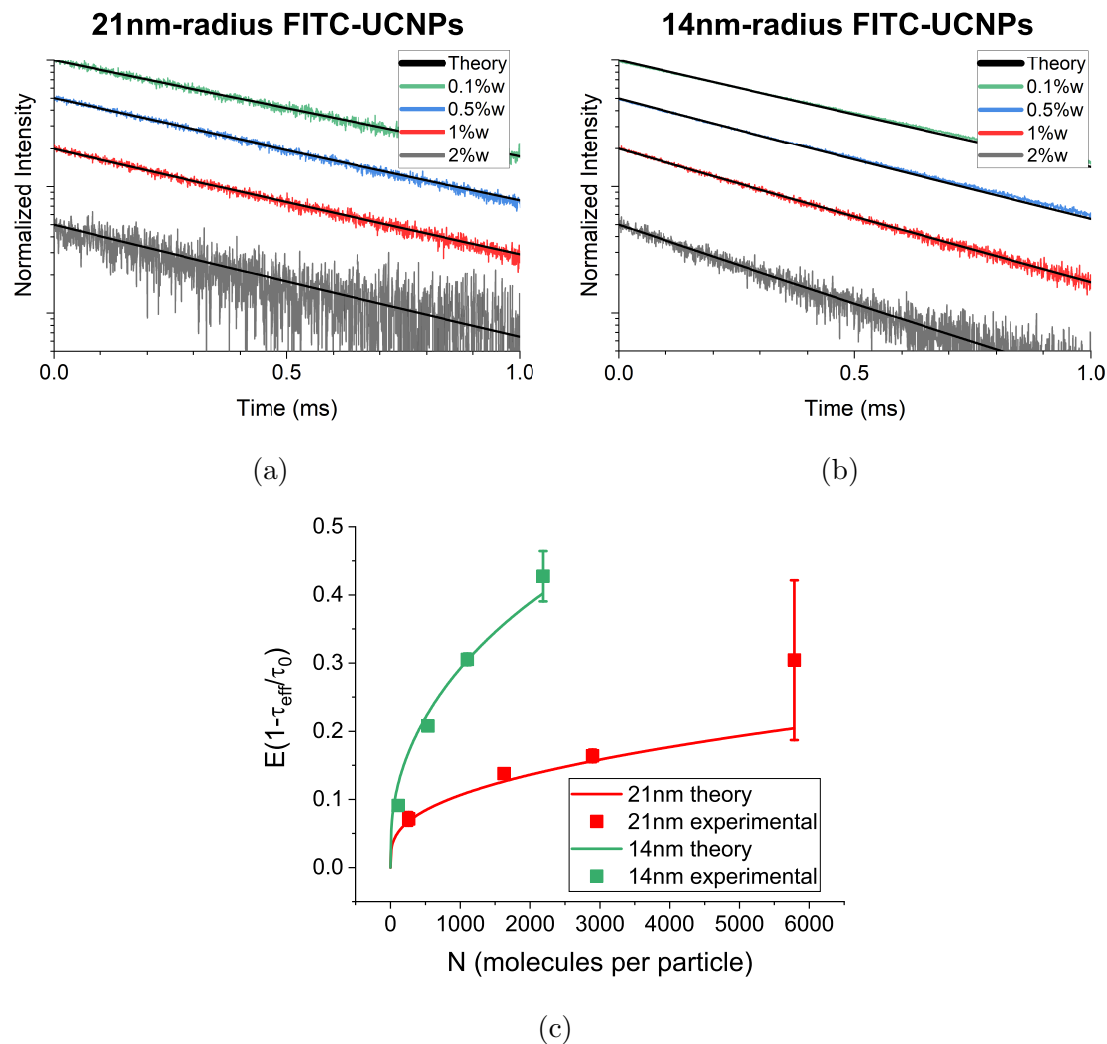


FIG. 6: (a,b) Experimental and theoretical time decay profiles between 1 ms and 2 ms for FITC-UCNPs with different particle radius, and different weight concentrations of FITC. The measurements are offset to facilitate the reading of the plot. (c) FRET efficiency for both UCNP sizes as a function of FITC loading. FRET efficiency increases with smaller particle size and higher FITC loading. The experimental FITC-UCNP effective time constants (τ_{eff} , see SI 6) are obtained by integrating the transient PL curves shown in Figures 6a and 6b over time. Theoretical effective time constants are calculated by integrating Equation S.7 over time. Error bars are estimated from the noise in the normalized PL measurements after the UCNPs have fully decayed.

calculate the FRET efficiency. The FRET efficiency is given by:

$$E = 1 - \frac{\tau_{\text{eff}}}{\tau_0} \quad (8)$$

where τ_{eff} is the effective time constant obtained from integrating the FITC-UCNP transient PL curve over time and τ_0 is the time constant of the UCNP with no FITC.

Figure 6c shows the measured FRET efficiency for the various UCNP sizes and FITC loadings studied. The error bars are estimated from the noise in the normalized transient PL curves once the UCNPs have fully decayed. As expected, FRET efficiency is higher for smaller particle size and higher FITC loadings. We also plot the theoretical FRET efficiency for both sizes as a function of FITC loading which we obtain by integrating Equation S.7 over time with appropriate choices of number of FITC molecules, particle radius, and Förster radius. Both the fits in Figures 6a and 6b and the extracted efficiencies in Figure 6c demonstrate excellent agreement between the experimental results and theory.

B. Design of an ideal FRET-based sensor

Finally, we consider how the model can be applied to design the optimal biosensor. The relevant parameters to consider are the number of acceptors attached to the surface of the nanoparticle, the Förster radius of the donor-acceptor pair, and the radius of the particle. While, as we have shown in this paper, the number of acceptor molecules can be tuned, eventually there is a hard limit for a given particle size of how many molecules you can attach onto the particle. Förster radius can be varied by different choices of acceptor molecules and rare earth ions. However, there might be limited options available for acceptor molecules that react appropriately to the target being sensed. Similarly, there is only a finite number of emission wavelengths from the lanthanide ions. The radius of the nanoparticle in contrast can be very easily tuned and there has been an abundance of work showing a variety of UCNP particle sizes with various shell thicknesses grown over them as well^{13,19,23,42–46}.

Figure 7a shows the calculated FRET efficiency as a function of the ratio of Förster radius to particle radius, η . We assume a surface coverage of 3000 molecules per particle. As seen in Figure 7a, for small ratios (small Förster radius or large particle size), the particle experiences minimal changes, as the effects of FRET do not extend far into the particle. At large ratios (large Förster radius or small particle size), all the ions within the particle experience FRET so the FRET efficiency is high, resulting in the largest drop in luminescence intensity.

Recall that in a FRET-based sensor, the dye molecule absorption spectrum changes as

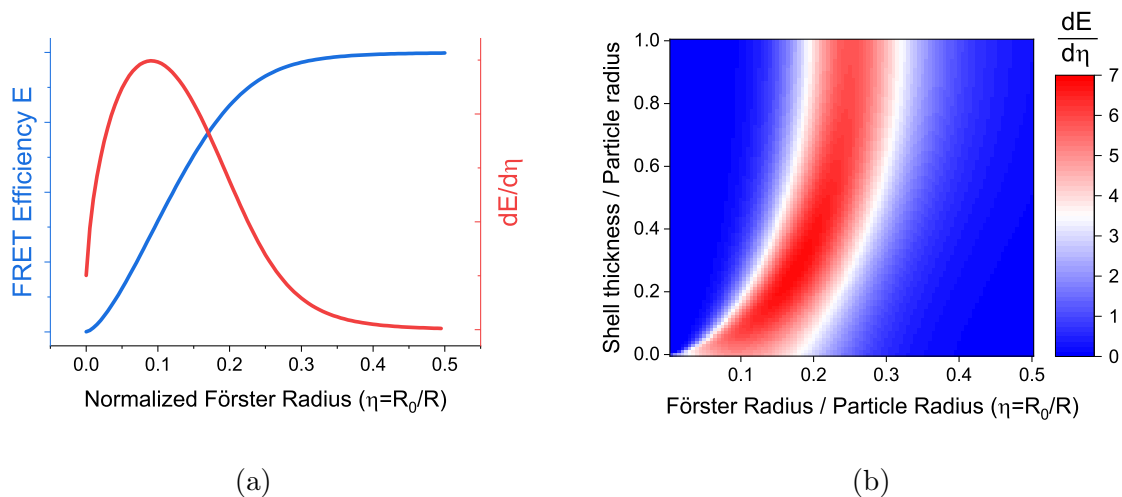


FIG. 7: Design of an optimal biosensor. (a) FRET efficiency, as defined in equation S.6, as a function of the normalized Förster radius $\eta = R_0/R$. A larger normalized radius (higher Förster radius or smaller particle radius) results in a higher FRET efficiency. Also, derivative of that FRET efficiency with respect to the normalized Förster radius η .

Sensitivity of the biosensor is maximized when this derivative is maximized. (b) Dependence of the derivative of the FRET efficiency defined in equation S.6 with respect to the shell thickness and the Förster radius. Even with an inert shell, comparable levels of sensitivity to the simple core-only structure can be achieved.

a function of the solvent. This corresponds directly to a change in Förster radius (see SI 1) and thus a change in the ratio of Förster radius to particle size. Therefore, an optimally designed biosensor should experience the largest change in intensity for a given change in ratio. The derivative of the curve in Figure 7a must be maximized. From Figure 7a, which shows this derivative, we find that the derivative reaches maximum at a ratio around 0.1. Consequently, for a surface coverage of 3000 molecules per particle, one should use a UCNP radius that is ten times the Förster radius of the dye-UCNP system. Figure 7b extends this line of thinking to a core-shell configuration. Here, we present a surface plot of the same derivative in Figure 7a but also consider various ratios of inert shell thickness to active core radius. We find that a similar optimal point occurs for core-shell configurations as well, albeit at a slightly smaller radius than the simple UCNP case. Note that the maximum derivative in the core-shell case is of a similar value to the core case. Thus, using a core shell UCNP with brighter emission does not necessarily compromise the sensitivity of your

biosensor, if the size of the biosensor is chosen appropriately.

IV. CONCLUSION

By extending the FRET theory for a simple donor-acceptor pair model, we have developed a model to predict the changes due to FRET for a system comprised of a sphere of donors surrounded by a surface layer of acceptors. This complex system is more appropriate for describing dye-conjugated UCNP sensors which work via nonradiative energy transfer between the dye and UCNP. The extended model is necessary in order to fully capture the competition between the rare-earth ions close to the edge of the UCNP that experience large changes due to FRET and the ions close to the core of the UCNP that experience minimal changes due to FRET.

Our model was verified by comparing theoretical predictions to a system of Tm^{3+} UCNPs conjugated with FITC, a system that has been previously used as a sensor for pH. Varying both the amount of FITC conjugated onto the UCNP surface and the radius of the UCNP, we observed a change in lifetimes due to FRET that matches the predicted change using our theory. Our model is appropriate for any FRET-based sensor that has the same geometry and can be easily extended to more complicated geometries such as core-shell structures. The overall change due to FRET for such geometries was found to depend only on the radius of the particle, the Förster radius, and of the number of acceptors attached to the surface. Using our model, we showed that it is possible to find the optimal size of a particle, for a fixed Förster radius and surface density, that maximizes the sensitivity. This optimal size for a core-shell structure was found to have comparable sensitivity to an optimized core-only structure.

V. MATERIALS

Anhydrous YCl_3 , YbCl_3 , TmCl_3 , Oleic Acid (technical grade, 90%) (OA), 1-octadecene (technical grade, 90%), ammonium fluoride (NH_4F), polyethylenimine (PEI solution, 50%wt. in H_2O , average $M_n \approx 1800$), and FITC (Fluorescein isothiocyanate isomer 1) were bought from Sigma-Aldrich. Nitrosonium Tetrafluoroborate (NOBF_4) and solid sodium hydroxide (NaOH) pellets were purchased from Fisher Scientific. All chemicals were used as received without further purification.

VI. METHODS

A. Synthesis of Tm-UCNPs

To synthesize 40 nm UCNPs, we adopted a thermal coprecipitation method where we dissolved rare earth chlorides in an octadecene/oleic acid solution⁴⁷. A highly detailed description of the synthesis methodology can be found in the supplementary information (see SI 4a and 4b). The same methodology was used to create the smaller 14nm particles, but with some of the YCl₃ precursor replaced with GdCl₃.

B. Synthesis of FITC-conjugated UCNPs

The fluorescent FITC dye was conjugated using the ligand exchange method developed by Dong et al.⁴⁸. First, OA-coated UCNPs were dispersed in hexane, then added dropwise to a DMF solution of NOBF₄ while stirring. After 45 minutes, the top hexane layer was extracted, and the particles were collected by centrifuging the DMF phase. The particles were then redispersed in DMF and added to a DMF solution of PEI while stirring. After letting the solution mix overnight, the particles were again collected via centrifugation and redispersed in DMF. These particles were finally added to a DMF solution of FITC, left to react for 24 hours, and collected via centrifugation. A detailed description of the ligand exchange procedure, including masses and centrifuge speeds, can be found in the Supplementary Information (see section SI 4c).

VII. METHODS FOR THE MEASUREMENTS

In the transient PL measurements, an excitation laser source (Thorlabs L980P200) was modulated by a rectangular pulse generated by a function generator (Wavetek model 166). The duty ratio, pulse duration, and voltage amplitude were set appropriately, so that the transient PL had enough time to reach the steady state. In this particular scenario, we defined a period of 10 ms.

The emitted PL from the solutions was collected by a convex lens, and imaged by a 4f system of lenses into a monochromator (Sciencetech 9057F) equipped with a visible photomultiplier tube (Hamamatsu H11461P-11 PMT). Finally, a photon counter (Stanford Research

Systems SR430) was used to convert the photomultiplier tube's output to digital transient waveforms, that were recorded and post-processed by using our custom software.

The FITC absorption curves were obtained by using a spectrophotometer (Shimadzu UV-Vis-NIR spectrophotometer UV-3101). TEM images of the UCNPs were obtained using a Tecnai T12 Spirit 120kV Electron Microscope. Particle size was calculated by averaging across several images.

VIII. SUPPLEMENTARY MATERIAL

See supplementary material for additional details of the theoretical model and material preparation conditions.

IX. ACKNOWLEDGEMENTS

This work was supported in part by the National Science Foundation (DMR-1420736, CBET 2029559).

X. DATA AVAILABILITY

The data that support the findings of this study are available from the corresponding author upon reasonable request.

REFERENCES

- ¹B. Zhou, L. Yan, J. Huang, X. Liu, L. Tao, and Q. Zhang, "Nir ii-responsive photon upconversion through energy migration in an ytterbium sublattice," *Nature Photonics* **14**, 760–766 (2020).
- ²D. K. Chatterjee, A. J. Rufaihah, and Y. Zhang, "Upconversion fluorescence imaging of cells and small animals using lanthanide doped nanocrystals," *Biomaterials* **29**, 937–943 (2008).
- ³Q. Liu, W. Feng, T. Yang, T. Yi, and F. Li, "Upconversion luminescence imaging of cells and small animals," *Nature protocols* **8**, 2033–2044 (2013).

- ⁴W. Zheng, D. Tu, P. Huang, S. Zhou, Z. Chen, and X. Chen, “Time-resolved luminescent biosensing based on inorganic lanthanide-doped nanoprobe,” *Chemical Communications* **51**, 4129–4143 (2015).
- ⁵C. Lee, E. Z. Xu, Y. Liu, A. Teitelboim, K. Yao, A. Fernandez-Bravo, A. M. Kotulska, S. H. Nam, Y. D. Suh, A. Bednarkiewicz, *et al.*, “Giant nonlinear optical responses from photon-avalanching nanoparticles,” *Nature* **589**, 230–235 (2021).
- ⁶C. Wang, L. Cheng, and Z. Liu, “Drug delivery with upconversion nanoparticles for multifunctional targeted cancer cell imaging and therapy,” *Biomaterials* **32**, 1110–1120 (2011).
- ⁷L. Cheng, K. Yang, Y. Li, J. Chen, C. Wang, M. Shao, S.-T. Lee, and Z. Liu, “Facile preparation of multifunctional upconversion nanoprobe for multimodal imaging and dual-targeted photothermal therapy,” *Angewandte Chemie* **123**, 7523–7528 (2011).
- ⁸L. He, M. Brasino, C. Mao, S. Cho, W. Park, A. P. Goodwin, and J. N. Cha, “Dna-assembled core-satellite upconverting-metal-organic framework nanoparticle superstructures for efficient photodynamic therapy,” *Small* **13**, 1700504 (2017).
- ⁹L. He, J. Dragavon, S. Cho, C. Mao, A. Yildirim, K. Ma, R. Chattaraj, A. P. Goodwin, W. Park, and J. N. Cha, “Self-assembled gold nanostar — $\text{NaYF}_4: \text{Yb/Er}$ clusters for multimodal imaging, photothermal and photodynamic therapy,” *Journal of Materials Chemistry B* **4**, 4455–4461 (2016).
- ¹⁰S. K. Cho, L.-J. Su, C. Mao, C. D. Wolenski, T. W. Flaig, and W. Park, “Multifunctional nanoclusters of $\text{NaYF}_4: \text{Yb}^{3+}, \text{Er}^{3+}$ upconversion nanoparticle and gold nanorod for simultaneous imaging and targeted chemotherapy of bladder cancer,” *Materials Science and Engineering: C* **97**, 784–792 (2019).
- ¹¹M. Kumar and P. Zhang, “Highly sensitive and selective label-free optical detection of dna hybridization based on photon upconverting nanoparticles,” *Langmuir* **25**, 6024–6027 (2009).
- ¹²P. Zhang, S. Rogelj, K. Nguyen, and D. Wheeler, “Design of a highly sensitive and specific nucleotide sensor based on photon upconverting particles,” *Journal of the American Chemical Society* **128**, 12410–12411 (2006).
- ¹³P. Alonso-Cristobal, P. Vilela, A. El-Sagheer, E. Lopez-Cabarcos, T. Brown, O. Muskens, J. Rubio-Retama, and A. Kanaras, “Highly sensitive dna sensor based on upconversion nanoparticles and graphene oxide,” *ACS applied materials & interfaces* **7**, 12422–12429 (2015).

- ¹⁴L. Zhao, J. Peng, M. Chen, Y. Liu, L. Yao, W. Feng, and F. Li, “Yolk–shell upconversion nanocomposites for IRET sensing of cysteine/homocysteine,” *ACS Applied Materials & Interfaces* **6**, 11190–11197 (2014).
- ¹⁵Y. Zhang, Y. Tang, X. Liu, L. Zhang, and Y. Lv, “A highly sensitive upconverting phosphors-based off–on probe for the detection of glutathione,” *Sensors and Actuators B: chemical* **185**, 363–369 (2013).
- ¹⁶T. Guo, Q. Deng, G. Fang, Y. Yun, Y. Hu, and S. Wang, “A double responsive smart upconversion fluorescence sensing material for glycoprotein,” *Biosensors and Bioelectronics* **85**, 596–602 (2016).
- ¹⁷J. Zhang, B. Li, L. Zhang, and H. Jiang, “An optical sensor for Cu(II) detection with upconverting luminescent nanoparticles as an excitation source,” *Chemical Communications* **48**, 4860–4862 (2012).
- ¹⁸H. Li and L. Wang, “Nayf4: Yb³⁺/Er³⁺ nanoparticle-based upconversion luminescence resonance energy transfer sensor for mercury (II) quantification,” *Analyst* **138**, 1589–1595 (2013).
- ¹⁹R. Wei, Z. Wei, L. Sun, J. Z. Zhang, J. Liu, X. Ge, and L. Shi, “Nile red derivative-modified nanostructure for upconversion luminescence sensing and intracellular detection of Fe³⁺ and MR imaging,” *ACS Applied Materials & Interfaces* **8**, 400–410 (2016).
- ²⁰L.-N. Sun, H. Peng, M. I. Stich, D. Achatz, and O. S. Wolfbeis, “pH sensor based on upconverting luminescent lanthanide nanorods,” *Chemical Communications* , 5000–5002 (2009).
- ²¹R. Arppe, T. Näreoja, S. Nylund, L. Mattsson, S. Koho, J. M. Rosenholm, T. Soukka, and M. Schäferling, “Photon upconversion sensitized nanoprobe for sensing and imaging of pH,” *Nanoscale* **6**, 6837–6843 (2014).
- ²²C. Li, J. Zuo, L. Zhang, Y. Chang, Y. Zhang, L. Tu, X. Liu, B. Xue, Q. Li, H. Zhao, *et al.*, “Accurate quantitative sensing of intracellular pH based on self-ratiometric upconversion luminescent nanoprobe,” *Scientific reports* **6**, 38617 (2016).
- ²³M. K. Mahata and K. T. Lee, “Development of near-infrared sensitized core–shell–shell upconverting nanoparticles as pH-responsive probes,” *Nanoscale Advances* **1**, 2372–2381 (2019).
- ²⁴M. Strobl, T. Mayr, I. Klimant, and S. M. Borisov, “Photostable upconverting and downconverting pH sensors based on combination of a colorimetric NIR indicator and stable inor-

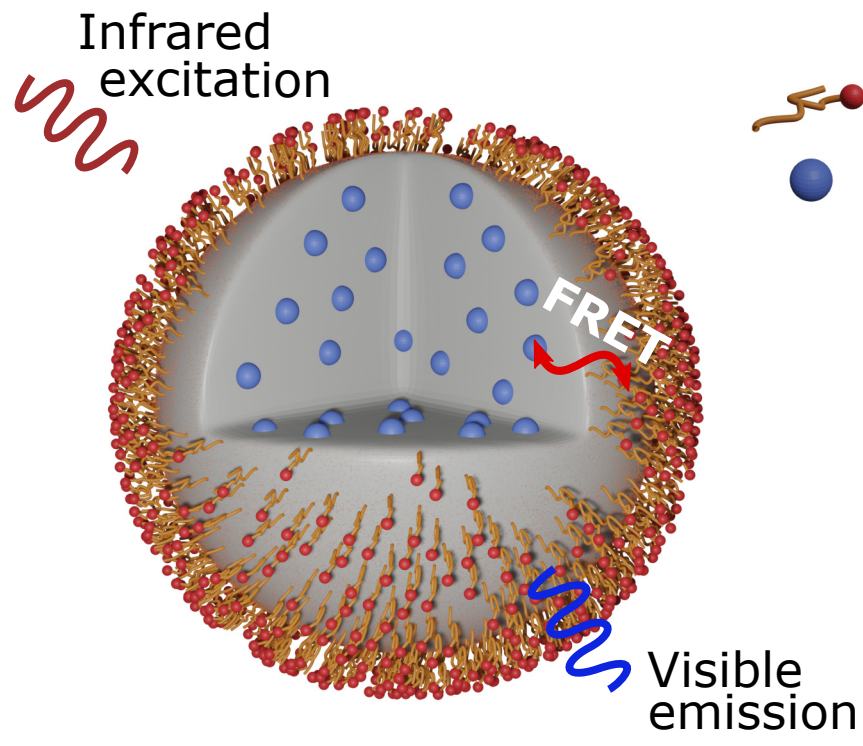
- ganic phosphors as secondary emitters,” *Sensors and Actuators B: Chemical* **245**, 972–979 (2017).
- ²⁵Q. Long, A. Fang, Y. Wen, H. Li, Y. Zhang, and S. Yao, “Rapid and highly-sensitive uric acid sensing based on enzymatic catalysis-induced upconversion inner filter effect,” *Biosensors and Bioelectronics* **86**, 109–114 (2016).
- ²⁶Y. Liu, Q. Ouyang, H. Li, Z. Zhang, and Q. Chen, “Development of an inner filter effects-based upconversion nanoparticles–curcumin nanosystem for the sensitive sensing of fluoride ion,” *ACS Applied Materials & Interfaces* **9**, 18314–18321 (2017).
- ²⁷B. Kumar, A. Murali, and S. Giri, “Upconversion nanoplatform for fret-based sensing of dopamine and ph,” *ChemistrySelect* **4**, 5407–5414 (2019).
- ²⁸S. Cheng, Q. Liu, X. Zhou, Y. Gu, W. Yuan, W. Feng, and F. Li, “Reversible ratiometric probe combined with the time-gated method for accurate in vivo gastrointestinal ph sensing,” *ACS Applied Materials & Interfaces* **12**, 25557–25564 (2020).
- ²⁹J. Xu, F. He, Z. Cheng, R. Lv, Y. Dai, A. Gulzar, B. Liu, H. Bi, D. Yang, S. Gai, *et al.*, “Yolk-structured upconversion nanoparticles with biodegradable silica shell for fret sensing of drug release and imaging-guided chemotherapy,” *Chemistry of Materials* **29**, 7615–7628 (2017).
- ³⁰Y. Ding, H. Zhu, X. Zhang, J.-J. Zhu, and C. Burda, “Rhodamine b derivative-functionalized upconversion nanoparticles for fret-based fe 3+-sensing,” *Chemical Communications* **49**, 7797–7799 (2013).
- ³¹C. E. Rowland, C. W. Brown III, I. L. Medintz, and J. B. Delehanty, “Intracellular fret-based probes: a review,” *Methods and applications in fluorescence* **3**, 042006 (2015).
- ³²Z. S. Pehlivan, M. Torabfam, H. Kurt, C. Ow-Yang, N. Hildebrandt, and M. Yüce, “Aptamer and nanomaterial based fret biosensors: a review on recent advances (2014–2019),” *Microchimica Acta* **186**, 563 (2019).
- ³³G. Bunt and F. S. Wouters, “Fret from single to multiplexed signaling events,” *Biophysical reviews* **9**, 119–129 (2017).
- ³⁴Q. Liu, Y. Zhang, C. S. Peng, T. Yang, L.-M. Joubert, and S. Chu, “Single upconversion nanoparticle imaging at sub-10 w cm- 2 irradiance,” *Nature photonics* **12**, 548–553 (2018).
- ³⁵C. Siefe, R. D. Mehlenbacher, C. S. Peng, Y. Zhang, S. Fischer, A. Lay, C. A. McLellan, A. P. Alivisatos, S. Chu, and J. A. Dionne, “Sub-20 nm core–shell–shell nanoparticles for bright upconversion and enhanced förster resonant energy transfer,” *Journal of the*

- American Chemical Society **141**, 16997–17005 (2019).
- ³⁶J. Zhou, C. Li, D. Li, X. Liu, Z. Mu, W. Gao, J. Qiu, and R. Deng, “Single-molecule photoreaction quantitation through intraparticle-surface energy transfer (i-set) spectroscopy,” *Nature communications* **11**, 1–8 (2020).
- ³⁷R. Deng, J. Wang, R. Chen, W. Huang, and X. Liu, “Enabling Förster resonance energy transfer from large nanocrystals through energy migration,” *Journal of the American Chemical Society* **138**, 15972–15979 (2016).
- ³⁸Y.-X. Wu, X.-B. Zhang, D.-L. Zhang, C.-C. Zhang, J.-B. Li, Y. Wu, Z.-L. Song, R.-Q. Yu, and W. Tan, “Quench-shield ratiometric upconversion luminescence nanoplatforM for biosensing,” *Analytical chemistry* **88**, 1639–1646 (2016).
- ³⁹S. Du, J. Hernández-Gil, H. Dong, X. Zheng, G. Lyu, M. Bañobre-López, J. Gallo, L.-d. Sun, C.-h. Yan, and N. J. Long, “Design and validation of a new ratiometric intracellular pH imaging probe using lanthanide-doped upconverting nanoparticles,” *Dalton Transactions* **46**, 13957–13965 (2017).
- ⁴⁰K. Schauenstein, G. Böck, and G. Wick, “Short time bleaching of fluorescein isothiocyanate. a possible parameter for the specific binding of conjugates in immunofluorescence.” *Journal of Histochemistry & Cytochemistry* **28**, 1029–1031 (1980), PMID: 6774008, <https://doi.org/10.1177/28.9.6774008>.
- ⁴¹D. Lu, C. Mao, S. K. Cho, S. Ahn, and W. Park, “Experimental demonstration of plasmon enhanced energy transfer rate in NaYF₄: Yb³⁺, Er³⁺ upconversion nanoparticles,” *Scientific reports* **6**, 1–11 (2016).
- ⁴²S. Melle, O. G. Calderón, M. Laurenti, D. Mendez-Gonzalez, A. Egatz-Gómez, E. López-Cabarcos, E. Cabrera-Granado, E. Díaz, and J. Rubio-Retama, “Förster resonance energy transfer distance dependence from upconverting nanoparticles to quantum dots,” *The Journal of Physical Chemistry C* **122**, 18751–18758 (2018).
- ⁴³Y. Ding, F. Wu, Y. Zhang, X. Liu, E. M. de Jong, T. Gregorkiewicz, X. Hong, Y. Liu, M. C. Aalders, W. J. Buma, *et al.*, “Interplay between static and dynamic energy transfer in biofunctional upconversion nanoplatforM,” *The journal of physical chemistry letters* **6**, 2518–2523 (2015).
- ⁴⁴V. Muhr, C. Würth, M. Kraft, M. Buchner, A. J. Baeumner, U. Resch-Genger, and T. Hirsch, “Particle-size-dependent Förster resonance energy transfer from upconversion nanoparticles to organic dyes,” *Analytical chemistry* **89**, 4868–4874 (2017).

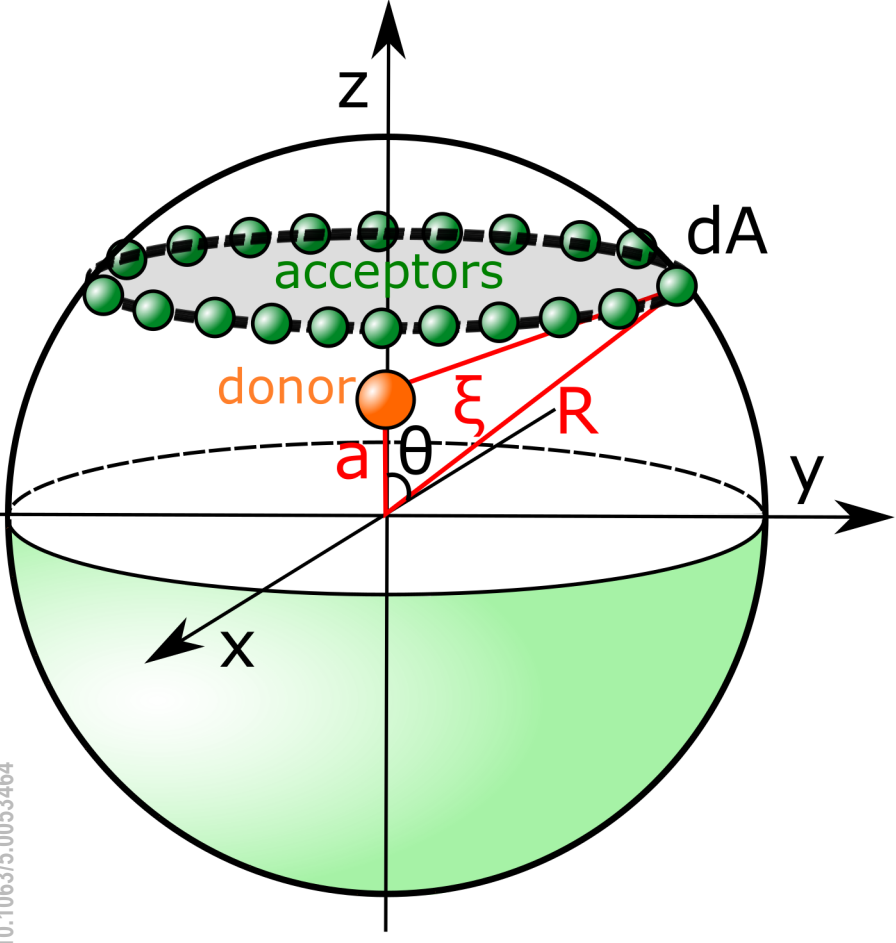
This is the author's peer reviewed, accepted manuscript. However, the online version of record will be different from this version once it has been copyedited and typeset.
PLEASE CITE THIS ARTICLE AS DOI: 10.1063/1.50053464

- ⁴⁵O. Dukhno, F. Przybilla, M. Collot, A. Klymchenko, V. Pivovarenko, M. Buchner, V. Muhr, T. Hirsch, and Y. Mély, “Quantitative assessment of energy transfer in up-converting nanoparticles grafted with organic dyes,” *Nanoscale* **9**, 11994–12004 (2017).
- ⁴⁶F. Wang, Y. Han, C. S. Lim, Y. Lu, J. Wang, J. Xu, H. Chen, C. Zhang, M. Hong, and X. Liu, “Simultaneous phase and size control of upconversion nanocrystals through lanthanide doping,” *nature* **463**, 1061–1065 (2010).
- ⁴⁷Z. Li and Y. Zhang, “An efficient and user-friendly method for the synthesis of hexagonal-phase Yb, Er/Tm nanocrystals with controllable shape and upconversion fluorescence,” *Nanotechnology* **19**, 345606 (2008).
- ⁴⁸A. Dong, X. Ye, J. Chen, Y. Kang, T. Gordon, J. M. Kikkawa, and C. B. Murray, “A generalized ligand-exchange strategy enabling sequential surface functionalization of colloidal nanocrystals,” *Journal of the American Chemical Society* **133**, 998–1006 (2011).

This is the author's peer reviewed, accepted manuscript. However, the online version of record will be different from this version once it has been copyedited and typeset.
PLEASE CITE THIS ARTICLE AS DOI: 10.1063/5.0053464

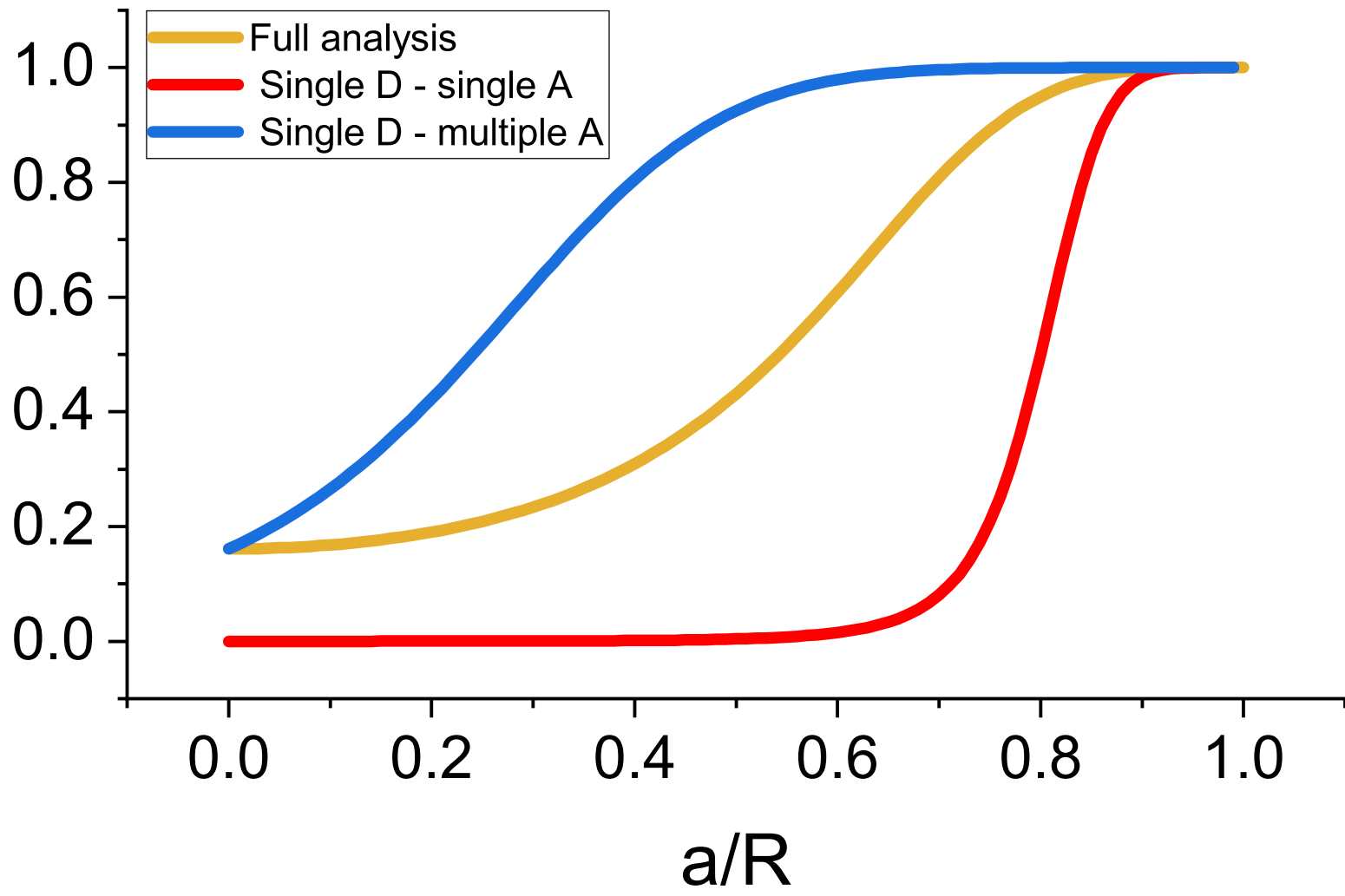


This is the author's peer reviewed, accepted manuscript. However, the online version of record will be different from this version once it has been copyedited and typeset.
PLEASE CITE THIS ARTICLE AS DOI: 10.1063/5.0053464

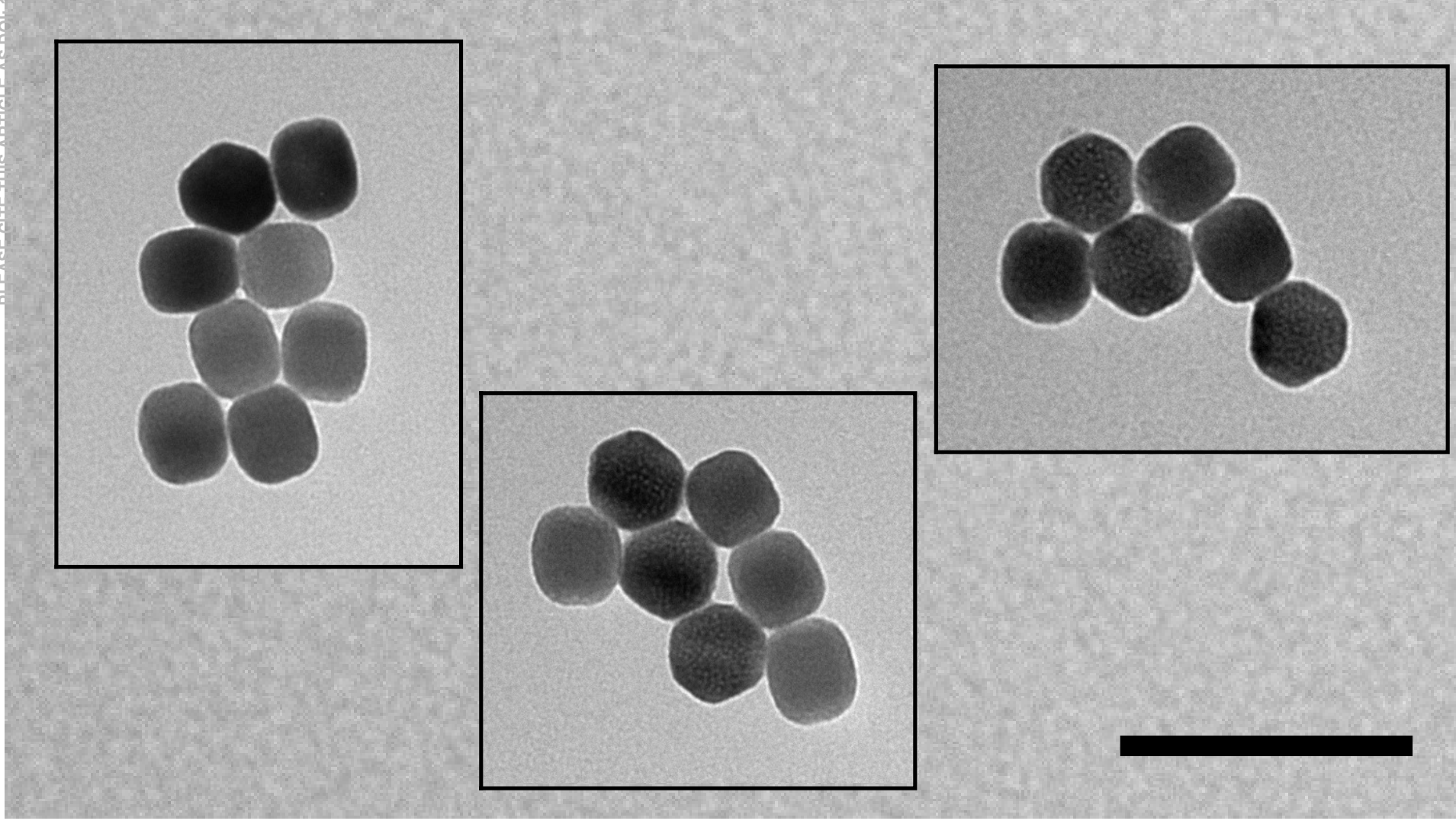


This is the author's peer reviewed, accepted manuscript. However, the online version of record will be different from this version once it has been copyedited and typeset.
PLEASE CITE THIS ARTICLE AS DOI: 10.1063/5.0053464

FRET Efficiency

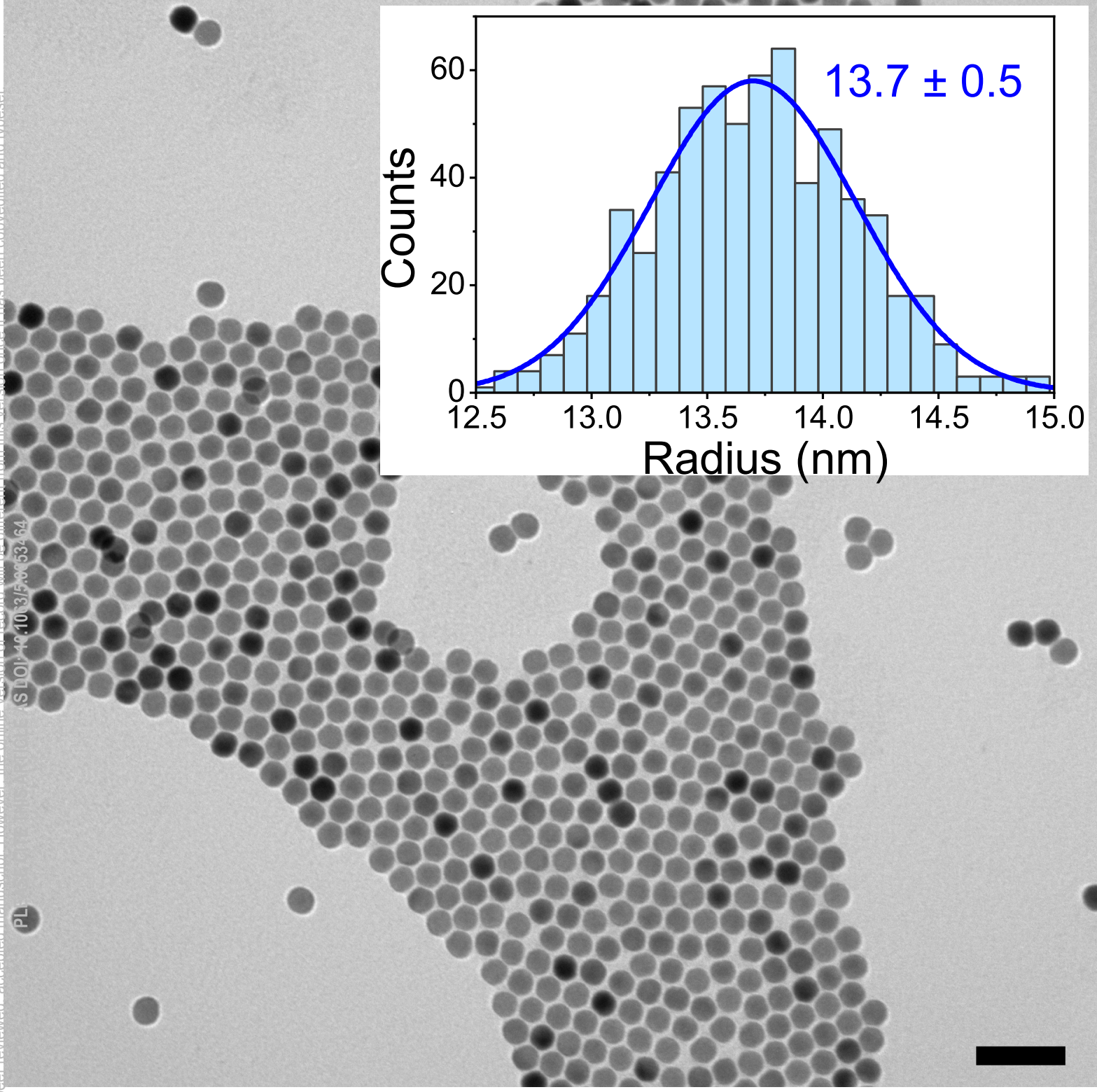


This is the author's peer reviewed, accepted manuscript. However, the online version of record will be different from this version once it has been copyedited and typeset.
PLEASE CITE THIS ARTICLE AS DOI: 10.1063/1.50053464



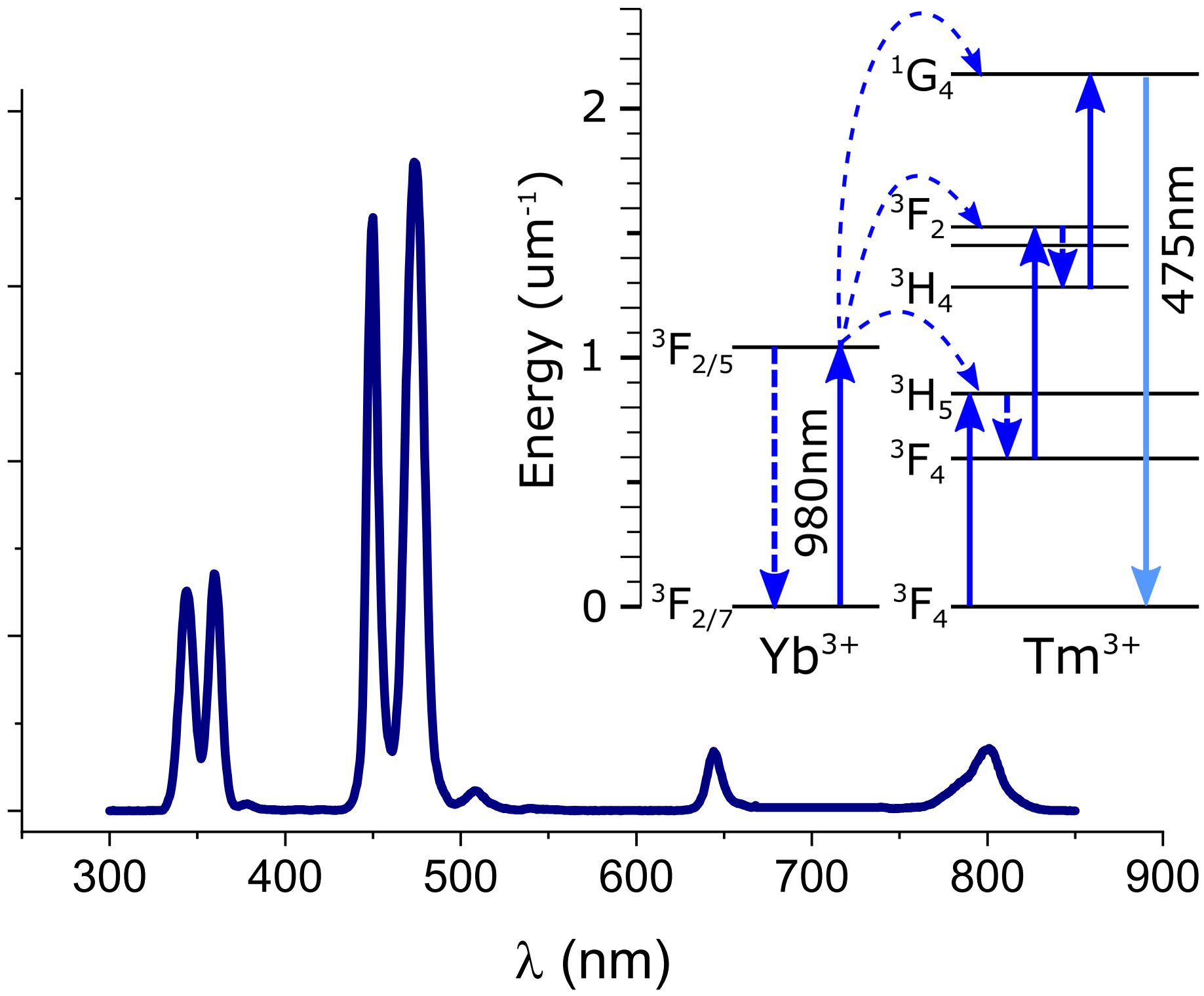
This is the author's peer-reviewed, accepted manuscript. However, the online version of record will be different from this version once it has been converted and typeset.

PL
DOI: 10.1063/1.5065346

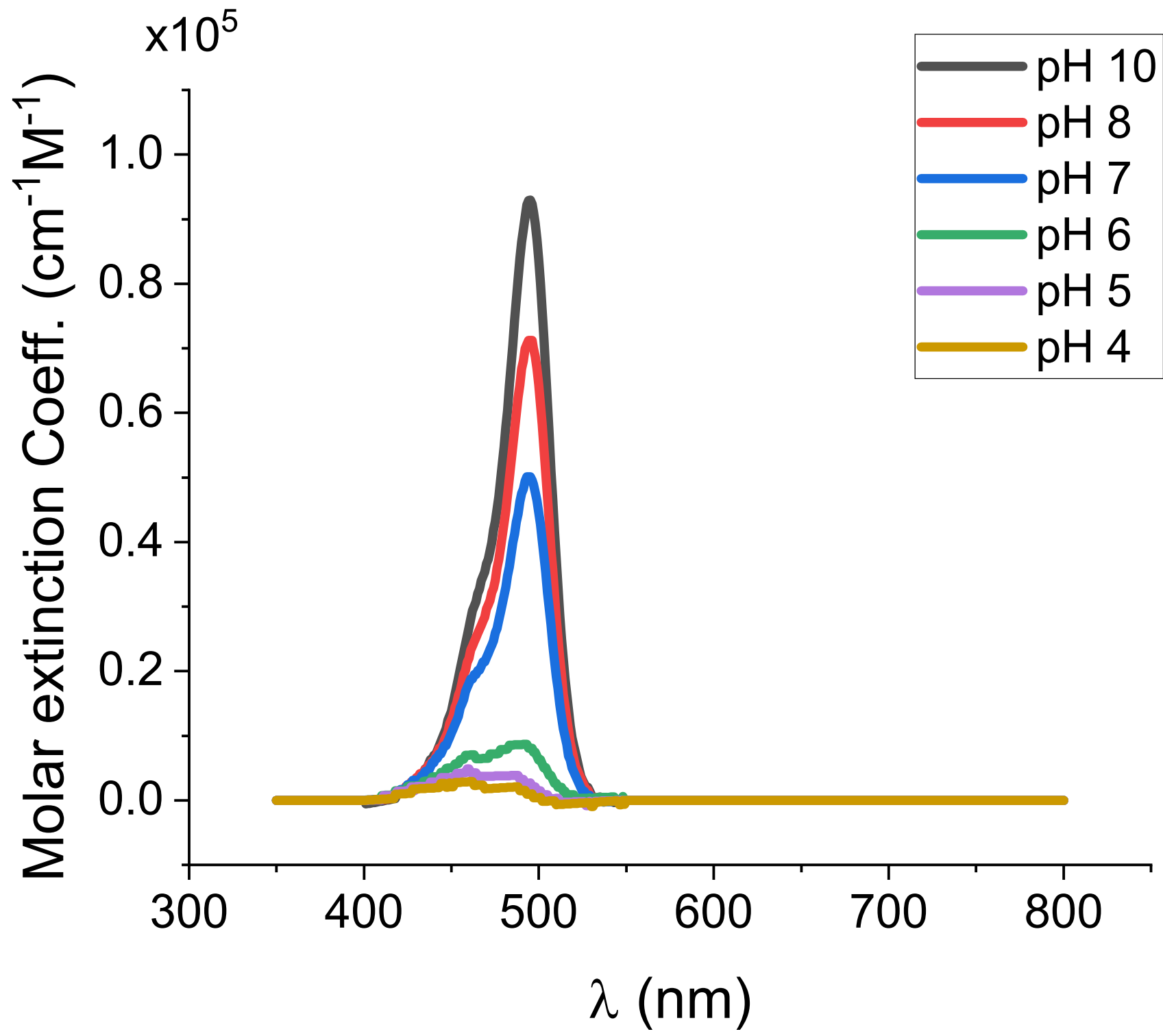


This is the author's peer reviewed, accepted manuscript. However, the online version of record will be different from this version once it has been copyedited and typeset.
PLEASE CITE THIS ARTICLE AS DOI: 10.1063/5.0053464

Emission Intensity

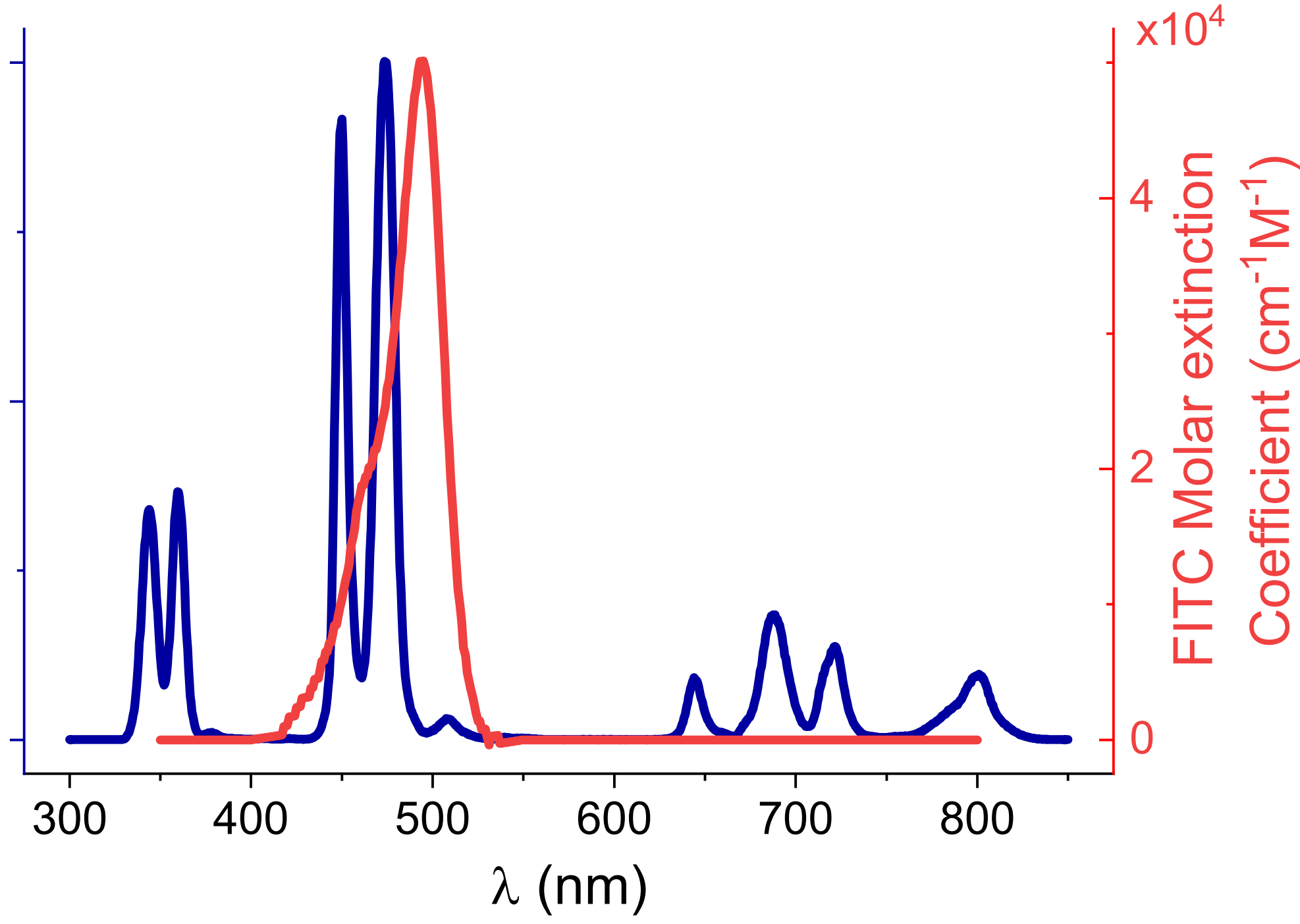


This is the author's peer reviewed, accepted manuscript. However, the online version of record will be different from this version once it has been copyedited and typeset.
PLEASE CITE THIS ARTICLE AS DOI: 10.1063/5.0053464



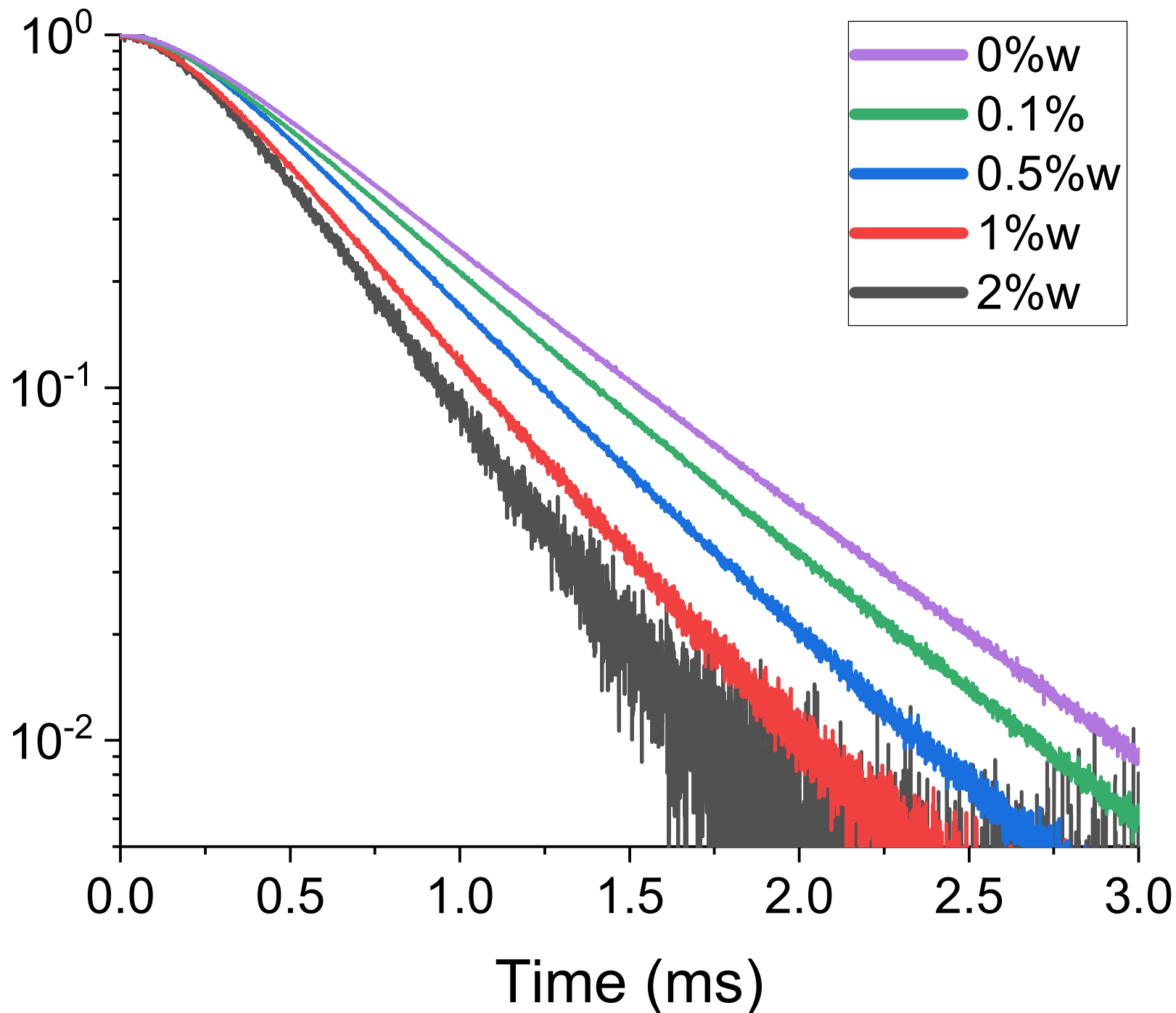
This is the author's peer reviewed, accepted manuscript. However, the online version of record will be different from this version once it has been copyedited and typeset.
PLEASE CITE THIS ARTICLE AS DOI: 10.1063/5.0053464

UCNPs Emission Intensity

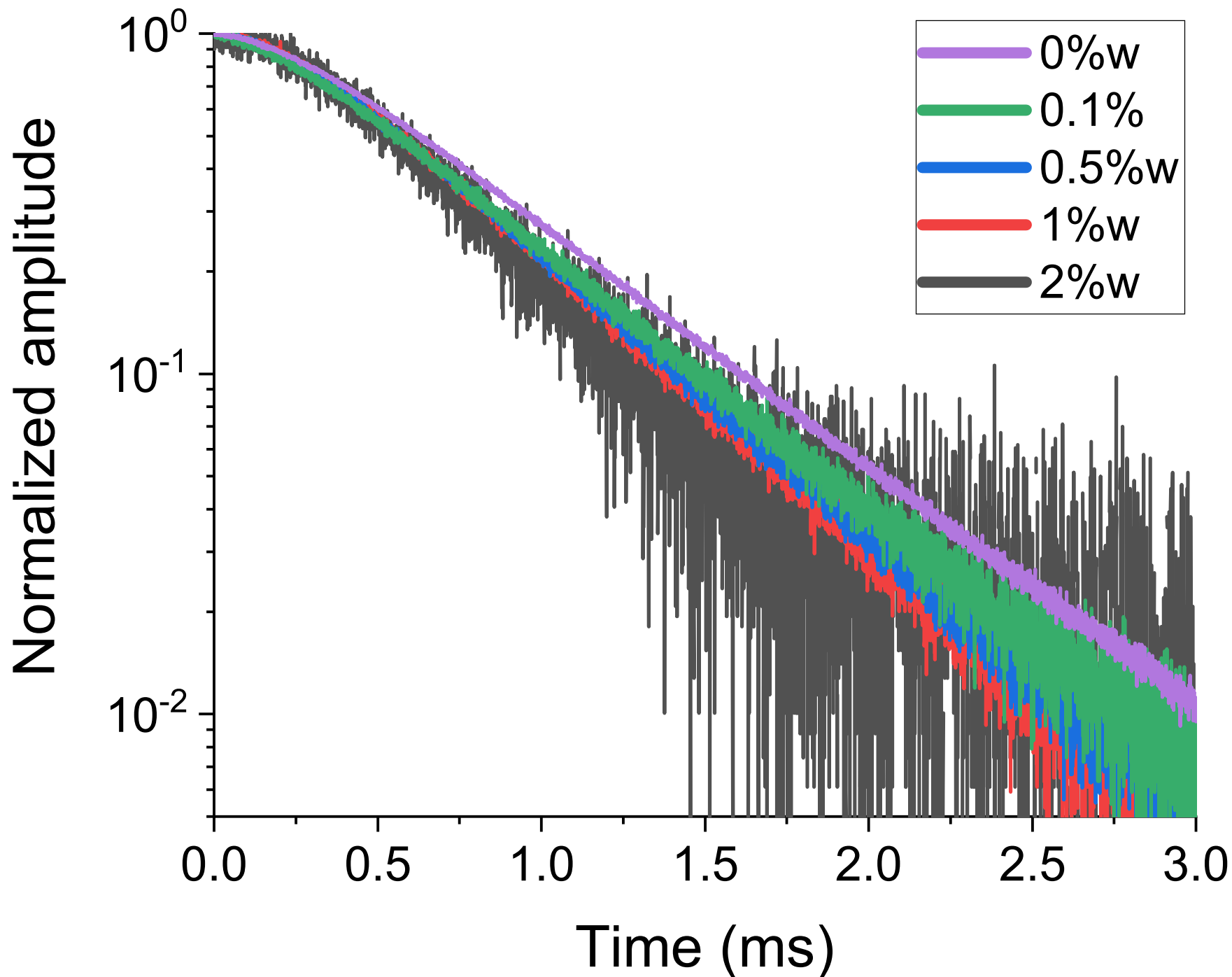


Normalized amplitude

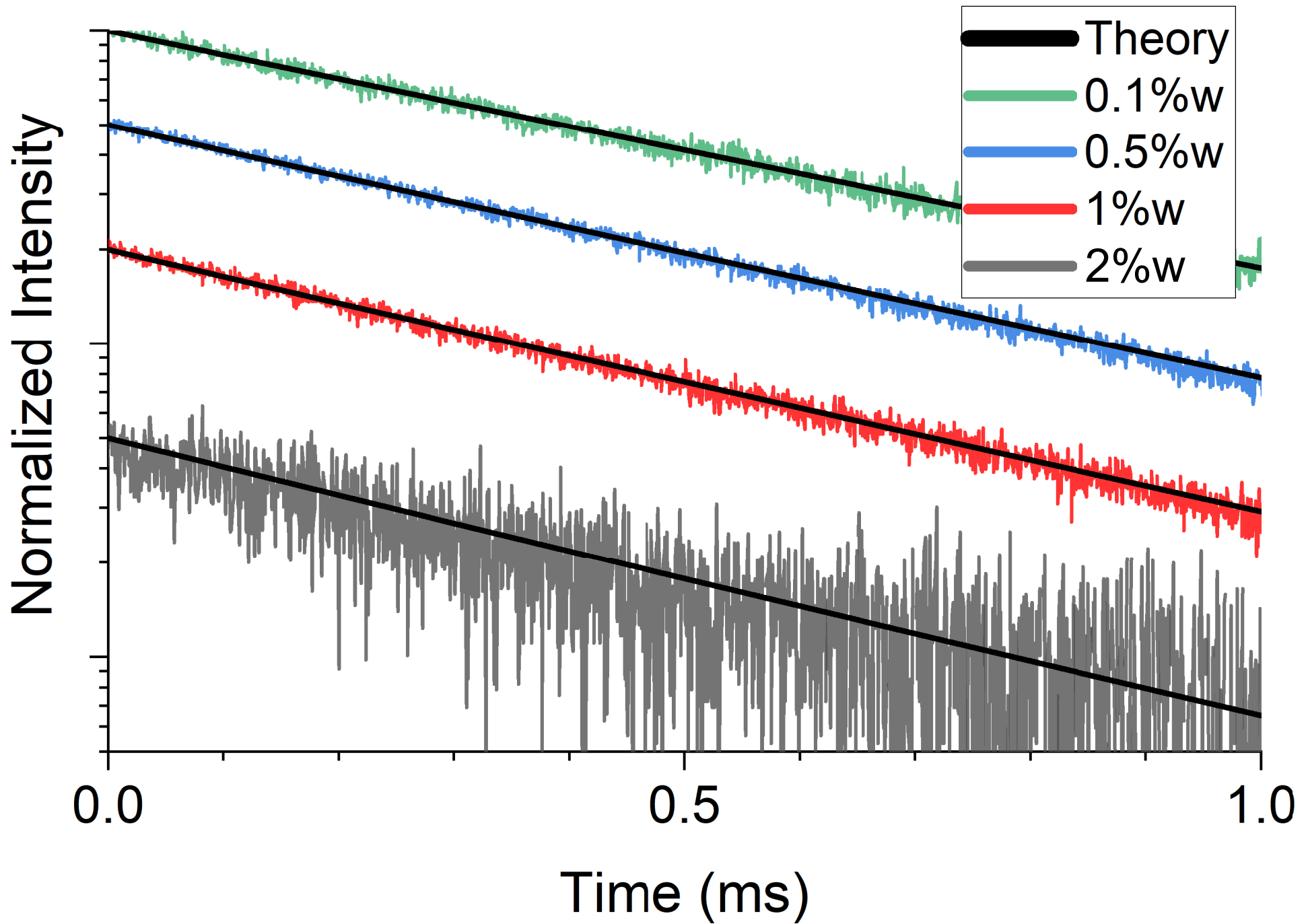
14nm-radius FITC-UCNPs



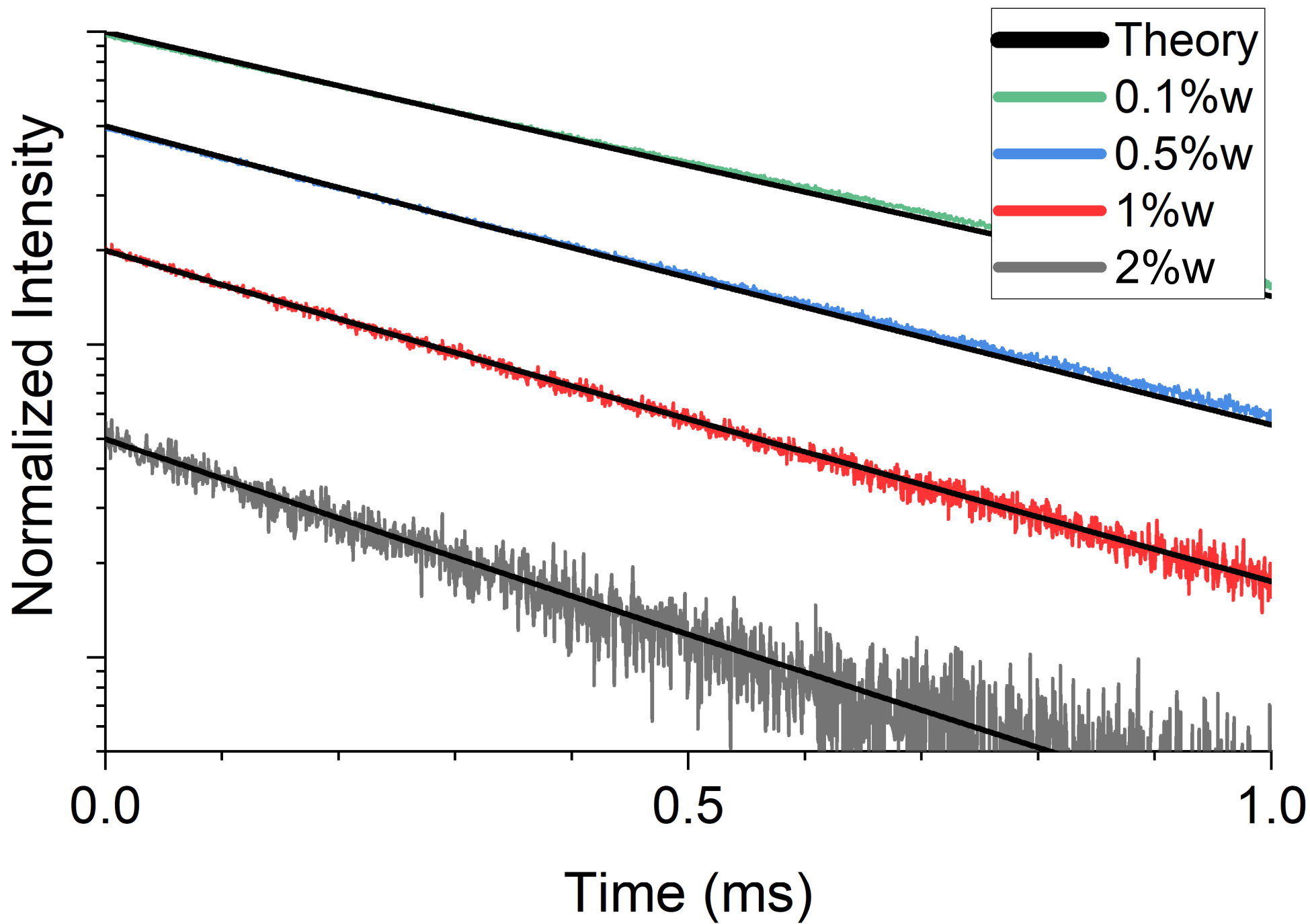
21nm-radius FITC-UCNPs



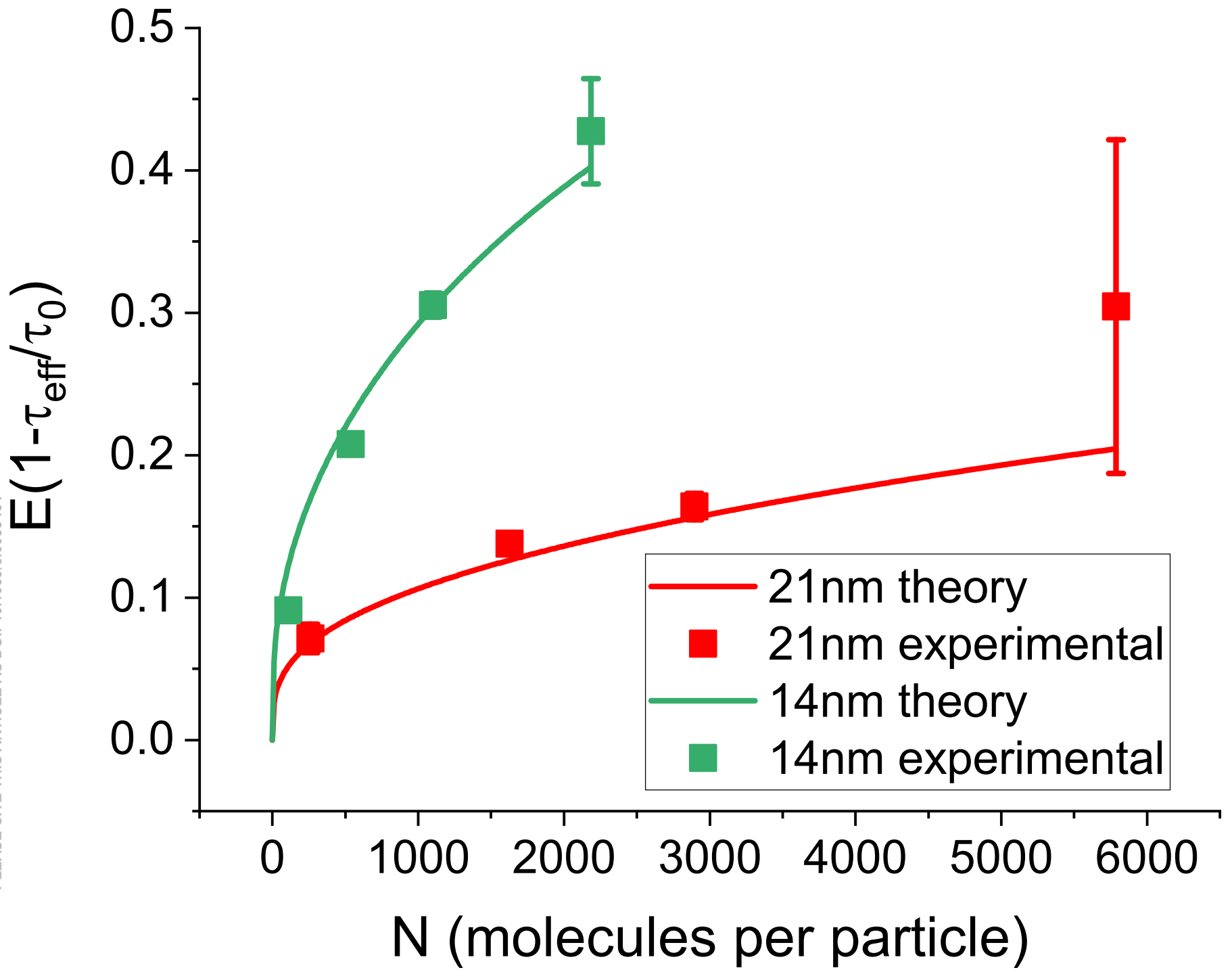
21nm-radius FITC-UCNPs



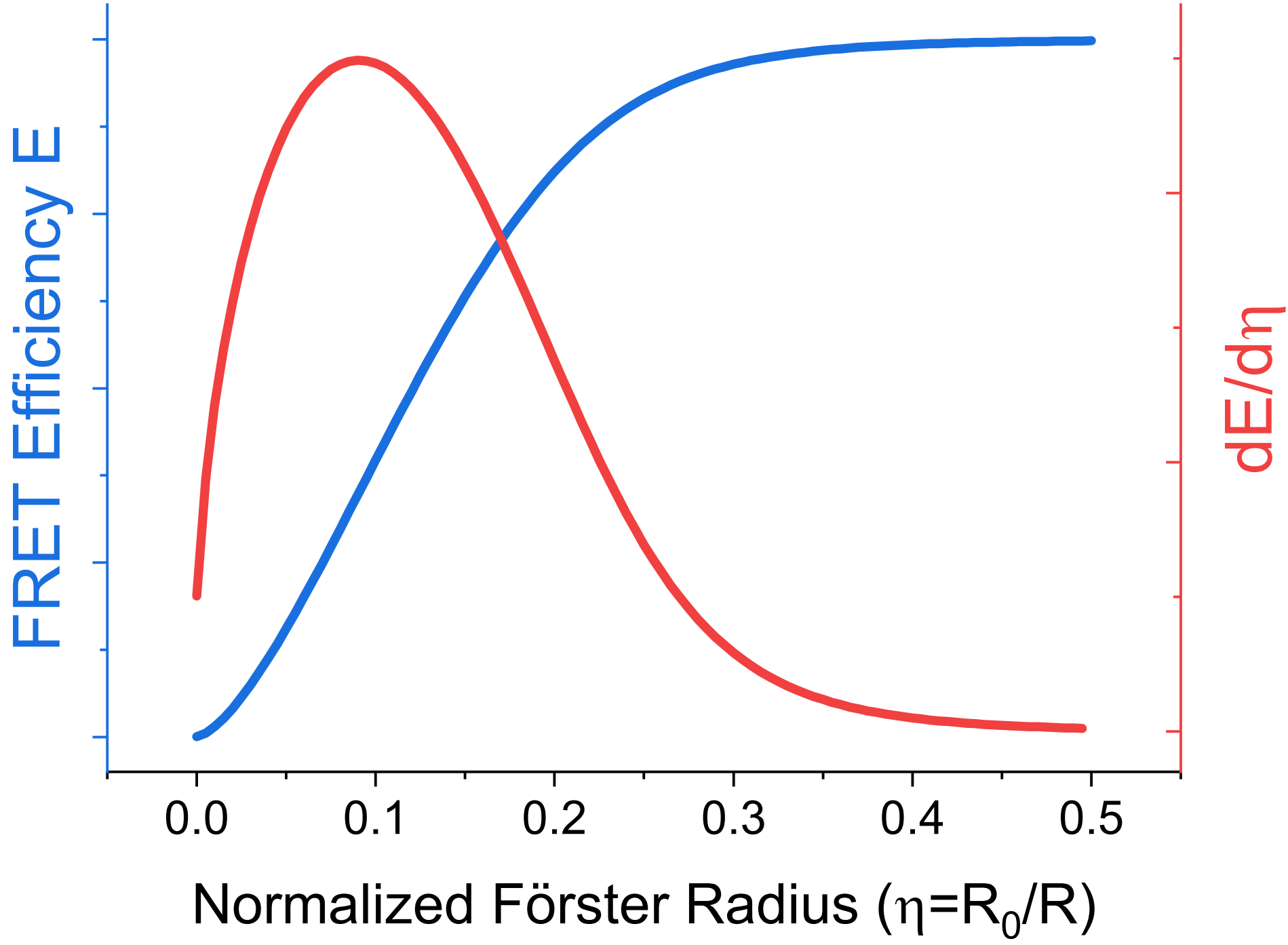
14nm-radius FITC-UCNPs



This is the author's peer reviewed, accepted manuscript. However, the online version of record will be different from this version once it has been copyedited and typeset.
PLEASE CITE THIS ARTICLE AS DOI: 10.1063/5.0053464



This is the author's peer reviewed, accepted manuscript. However, the online version of record will be different from this version once it has been copyedited and typeset.
PLEASE CITE THIS ARTICLE AS DOI: 10.1063/5.0053464



This is the author's peer reviewed, accepted manuscript. However, the online version of record will be different from this version once it has been copyedited and typeset.

PLEASE CITE THIS ARTICLE AS DOI: 10.1063/5.0053464

Shell thickness / Particle radius

